Inorganic Chemistry

pubs.acs.org/IC

Article

Mg_3Pt_2: Anionic Chains in a Eu_3Ga_2-Type Structure

Laura Agnarelli, Yurii Prots, Ulrich Burkhardt, Marcus Schmidt, Primož Koželj, Andreas Leithe-Jasper,* and Yuri Grin

Cite This: *Inorg. Chem.* 2021, 60, 13681−13690

Read Online

ACCESS | Metrics & More | Article Recommendations | Supporting Information

ABSTRACT: The binary phase Mg_3Pt_2 was prepared by direct reaction between the elements or by spark-plasma synthesis starting with MgH_2 and $PtCl_2$. The compound crystallizes in the monoclinic space group $C2/c$ with a = 7.2096(3) Å, b = 7.1912(4) Å, c = 6.8977(3) Å, and β = 106.072(3)° and is isotypic to Eu_3Ga_2. Analysis of the electron density within the quantum theory of atoms in molecules shows a significant charge transfer from Mg to Pt in agreement with the electronegativity difference. Further study of the chemical bonding with the electron localizability approach reveals the formation of Pt chains stabilized by a complex system of multicenter interactions involving Mg and Pt species. The metallic character of Mg_3Pt_2 is confirmed by electronic structure calculations and physical measurements.

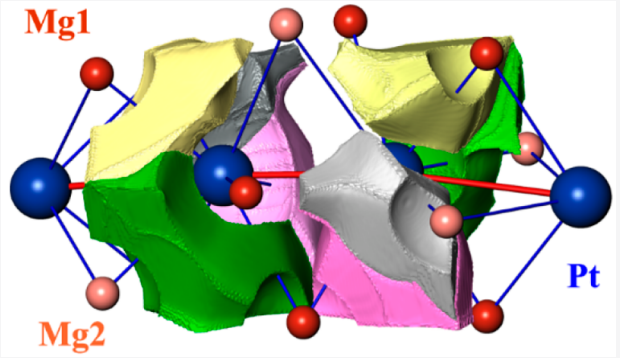

1. INTRODUCTION

The low density of Mg is considered to be a major advantage in manufacturing, where weight reduction is an issue of increasing importance.[1−3] This particularly applies to the automotive sector and its needs for new structural materials.[4] Light-weight Mg alloys with improved mechanical properties are therefore a scientific topic for applied and pure material sciences.[5−9] Alloying elements like aluminum, copper, and zinc, together with other transition metals or rare-earth metals, are added to Mg to improve its strength, ductility, and creep and corrosion resistance.[10,11] Besides the strong focus on structural applications, current research on Mg alloys as hydrogen-storage materials[12−14] and their application as biomaterials should also be strongly emphasized.[15,16] Pt-rich alkaline-earth-metal alloys currently attract interest as electrocatalytic materials for the oxygen reduction reaction in fuel cells.[17,18] We also note that the use of Mg in extracting Pt from electronic or used-catalysator scrap has also been envisioned.[19] Mg is a chemically reactive element, and it easily interacts with the alloying constituents, giving rise to the formation of intermetallic compounds.[20−23] Besides their technological importance, exploring intermetallic compounds of Mg, their phase equilibria, and their structure−property relationships has been of general interest to the solid-state physics and chemistry community.[21,24−37] The high affinity of Mg to Pt metals[38] gives rise to a very variable structural chemistry,[39,40] as has been elaborated for the Mg−Rh,[41−46] Mg−Ir,[46−53] and several Mg−Pd[54−63] systems. For the Mg−Pt system, no phase diagram is reported in the literature; however, several intermetallic phases have already been described. The MgPt phase crystallizes with the FeSi structure type.[56] Exposing Li_2MgPt to hydrogen yields LiH and MgPt, which instead crystallizes with the CuAu structure type.[64] A homogeneous solid solution forms around the Mg_6Pt composition. The Mg_3Pt compound crystallizes with the Na_3As structure type.[65] In another investigation, however, Mg_3Pt was found to crystallize with the Cu_3P type (a superstructure of Na_3As).[66] Mg_2Pt, which adopts the tetragonal $CuAl_2$ structure type, was synthesized later.[67] Another two cubic phases, $MgPt_3$ and $MgPt_7$, were observed on the Pt-rich side of the Mg−Pt system.[68] A material with composition Mg_2Pt, for which the powder X-ray diffraction (PXRD) pattern was indexed with a C-centered monoclinic cell, was synthesized by the reaction between $PtCl_2$ and either solid or solubilized MgH_2 in organic solvents under mild conditions and a subsequent thermal treatment.[69] A tentative structure solution was based on the structure of the high-pressure modification of titanium in a subcell with the space group $C2/m$, mentioning that a cell having a 4 times larger volume has the symmetry of the space group $C2/c$.[70] In a thermodynamic study on the Mg−Pt system, the PXRD pattern of a phase with Mg_3Pt_2 composition was reported; however, not all of the reflections were indexed, and the structure of Mg_3Pt_2 remained unclear.[71]

Here we report a detailed study on the Mg_3Pt_2 phase, obtained either through a solid-state reaction between the

Received: July 2, 2021
Published: August 24, 2021

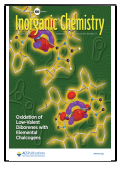

elements or by use of the spark-plasma synthesis, its crystal structure, and chemical bonding.

2. EXPERIMENTAL SECTION

Samples with nominal composition Mg_3Pt_2 were prepared from elemental Mg (granules, Alfa Aesar, 99.98 wt %) and Pt (powder, Alfa Aesar, 99.9 wt %). Pt powder was added to the already induction-melted Mg granules on the bottom of a Ta tube. The Ta tube was then welded and heated up to 1080 °C in a high-frequency furnace for about 5 min. The melted product was ground and compacted into a pellet, and the latter was placed in an alumina crucible and sealed into a Ta tube for annealing at 800 °C for 2 weeks in a tube furnace. The reaction product is brittle and gray with a metallic appearance and stable in air. The complete sample preparation was performed in an argon-filled glovebox [MBraun, $p(H_2O/O_2)$ < 0.1 ppm]. In an alternative way, the samples with nominal composition Mg_3Pt_2 were prepared from the powders $PtCl_2$ (ChemPur, 99.9 wt %), MgH_2 (in-house-synthesized[72]), and Pt (Alfa Aesar, 99.9 wt %) using the spark-plasma setup (SPS). Graphite dies with a diameter of 10 mm and a graphite lining were filled with approximately 1 g of the starting mixture and processed in an SPS-515 ET Sinter Lab apparatus (Fuji Electronic Industrial Co. Ltd., Tsurugashima, Japan) in an inert atmosphere. The reaction was performed in a vacuum (20 Pa) under uniaxial pressure (40 MPa), followed by slow cooling within the setup. The maximum temperature for the synthesis was constrained to 800 °C, reached within different rates, for a total preparation time of 130 min. After every experiment, the sample surface was cleaned from carbon and the product characterized by PXRD. The thermal behavior of the prepared materials was studied by differential scanning calorimetry (DSC; Netzsch DSC 404C Pegasus) using a closed Al_2O_3 crucible inside a sealed Ta ampule (see the Supporting Information). The chemical composition of the sample was determined by wavelength-dispersive X-ray spectroscopy (WDXS) performed on a Microprobe Cameca SX100 and scanning electron microscopy (SEM; Jeol JSM7800F) using Mg_2Sn and elemental Pt as standards for Mg and Pt, respectively. The magnetic susceptibility of Mg_3Pt_2 was measured on a Quantum Design MPMS-XL 7T magnetometer in the temperature range from 1.8 to 300 K, and the electrical resistivity was measured on a Quantum Design PPMS in the temperature range 1.9−300 K (see the Supporting Information). PXRD experiments were performed with a Guinier−Huber Image Plate Camera G670 and Cu Kα_1 radiation (λ = 1.54056 Å). Single crystals of Mg_3Pt_2 were selected from the crushed annealed samples. The splitters were glued to thin glass fibers and analyzed at room temperature using a Rigaku AFC7 diffraction system equipped with a Saturn 724+ CCD detector (Mo Kα radiation, λ = 0.71073 Å). The lattice parameters from the refinement of the PXRD and single-crystal X-ray diffraction data are in good agreement. Absorption correction was made by a multiscan procedure. All crystallographic calculations including the Rietveld refinement were performed with the program package *WinCSD*.[73] Details of the data collection and further crystallographic information are listed in Table 1.

3. CALCULATION PROCEDURES

The electronic structure calculation and bonding analysis were performed using the experimental values of the lattice parameters and atomic coordinates for Mg_3Pt_2 or employing the literature data for Eu_3Ga_2[74] and K_3Bi_2.[75] For Mg_3Pt_2, additional optimization of the atomic coordinates was performed to study the stability of the ELI-D maxima of the Pt−Pt bonds. The calculations were made with the all-electron, local orbital full−potential method (FPLO) within the local density approximation.[76] The f states of europium were treated as valence states. Perdew−Wang parametrization was employed.[77] Analysis of the chemical bonding in the position space[78,79] for all three compounds was performed by means of the electron localizability approach. For this purpose, the electron localizability indicator (ELI) in its ELI-D representation[80,81] and the electron density (ED) were calculated with a specialized module in the FPLO code.[82] The topology of ELI-D and ED was evaluated by means of the program *DGrid*.[83] The atomic charges from the ED and bond populations for bonding basins from ELI-D were obtained by the integration of ED and ELI-D, respectively, within the basins (space regions), bounded by zero-flux surfaces in the corresponding gradient field. This procedure follows the Quantum Theory of Atoms in Molecules (QTAIM).[84] Combined analysis of the ED and ELI-D yields basic information for the description of the bonding situation in solids, in particular for intermetallic compounds.[85−89]

Table 1. Crystallographic Data for Mg_3Pt_2

composition	Mg_3Pt_2
space group	$C2/c$
Pearson symbol	$mS20$
formula units per unit cell, Z	4
unit cell parameters[a]	
a (Å)	7.2096(3)
b (Å)	7.1912(4)
c (Å)	6.8977(3)
β (deg)	106.072(3)
unit cell volume, V (Å^3)	343.64(3)
calcd density, ρ (g cm^{-3})	8.940
cryst form	rectangular block
cryst size (μm^3)	12 × 25 × 25
diffraction syst	Rigaku AFC7
detector	Saturn 724+ CCD
radiation, λ	Mo Kα, 0.71073 Å
scan, step/degree, N(images)	φ, 0.8, 450
$2\theta_{max}$	60°
range in hkl	$-11 \le h \le 11$, $-5 \le k \le 10$, $-9 \le l \le 10$
abs corrn	multiscan
abs coeff (mm^{-1})	81.27
T(max)/T(min)	0.381/0.140
$N(hkl)$ measd	1257
$N(hkl)$ unique	495
R(int)	0.043
$N(hkl)$ obsd	436
observation criteria	$F(hkl) \ge 4\sigma[F(hkl)]$
R_F, R_W	0.039, 0.041
residual density (e Å^{-3})	−0.79/1.12

[a]The lattice parameters were refined from individual peak positions extracted from the PXRD pattern recorded with Cu Kα_1 radiation.

4. RESULTS AND DISCUSSION

4.1. Compound Formation. Using the direct reaction between the components, the existence of the Mg_3Pt_2 phase in the binary Mg−Pt system was confirmed. Its composition has been verified to be $Mg_{61(1)}Pt_{39(1)}$ from WDXS analysis. Once the exact composition of the phase was known, it was also synthesized following two alternative routes [reactions (1) and (2)] using the spark-plasma synthesis (Scheme 1).

Following reactions (1) and (2), Mg_3Pt_2 could not be obtained as a single phase because $Mg_{0.9}Pt_{1.09}$ was present as an impurity phase. From an experimental point of view, it was better to follow reaction (2) because the formation of $MgCl_2$ from reaction (1) required its removal from the reaction product. The lattice parameters of the product obtained after reaction (2)—a = 7.2093(4) Å, b = 7.1949(9) Å, c =

https://doi.org/10.1021/acs.inorgchem.1c01995
Inorg. Chem. 2021, 60, 13681−13690

Scheme 1. Alternative Routes for the Preparation of Mg_3Pt_2 Using the Spark-Plasma Synthesis with $PtCl_2$ and MgH_2 as Precursors (1) or Metallic Pt and MgH_2 (2)

$$2\ PtCl_2 + 4\ MgH_2 \longrightarrow Mg_3Pt_2 + MgCl_2 + 3\ H_{2(g)} + 2\ HCl_{(g)} \quad (1)$$

$$2\ Pt + 3\ MgH_2 \longrightarrow Mg_3Pt_2 + 3\ H_{2(g)} \quad (2)$$

6.8990(5) Å, and β = 106.078(8) deg—are within a few estimated standard deviations equal to the values of the product obtained from the elements (see below and Table 1). Thus, hydrogen uptake during the reaction can be excluded. From the DSC experiment, Mg_3Pt_2 decomposes congruently at 1214(1) °C (Figure S1).

4.2. Structure Determination. The PXRD pattern was indexed on the basis of a monoclinic unit cell [a = 7.2096(3) Å, b = 7.1912(4) Å, c = 6.8977(3) Å, and β = 106.072(3) deg]. All powder X-ray diffraction patterns showed small amounts [ca. 1.13(2)%] of the tetragonal phase $Mg_{0.9}Pt_{1.09}$ (isotypic to CuAu-type). This was also observed in the microstructure (Figure 1, inset).

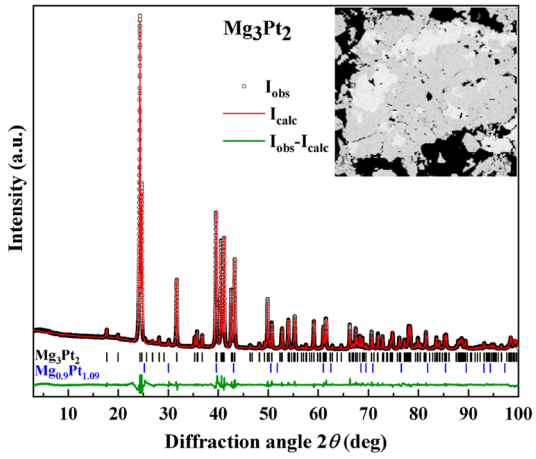

Figure 1. PXRD pattern of the Mg_3Pt_2 sample obtained by direct reaction of elemental metals, annealed at 800 °C for 2 weeks (Cu Kα_1 radiation). The peak positions of the Mg_3Pt_2 and $Mg_{0.9}Pt_{1.09}$ phases are marked with black and blue sticks, respectively [refined phase content: main phase, 98.87(16)%; minor phase, 1.13(2)%]. Inset: Microstructure of the reaction product using a backscattering detector in the SEM. The dark-gray regions represent Mg_3Pt_2, and the light-gray fields belong to the $Mg_{0.9}Pt_{1.09}$ phase.

Analysis of the diffraction intensities measured on a single crystal reveals systematic extinctions $h0l$ for h, l = 2n and $h + l$ = 2n for hkl reflections and indicates the possible space groups $C2/c$ and Cc. The crystal structure was solved and refined in the space group $C2/c$. The Pt atom and one of the Mg atoms are situated on 8f sites, and the second kind of Mg atom occupies the 4e site. The obtained composition Mg_3Pt_2 well matches the WDXS analysis. The displacement of Pt atoms is described in the anisotropic approximation; together with the isotropic description of the Mg displacement, this yields the R_F value of 0.041, and the anisotropic description of Mg slightly reduces the R value to 0.039 (Tables 1 and S1). Because of the strong difference in the scattering power, the anisotropic description of Mg is not stable in the refinement. The anisotropy of the Pt atoms can be understood as the influence of the Pt−Pt bonding in the chain (cf. bonding analysis below): the ellipsoids are elongated along the Pt−Pt bond lines. The "flat" ellipsoids of Mg are squeezed along the Pt−Mg bond lines, reflecting the high ionicity of the bonding. The refined atomic coordinates and equivalent displacement parameters are listed in Table 2, and the anisotropic displacement parameters are listed in Table S1. The crystallographic data are deposited in the ICSD database with deposition number 2089451.

Table 2. Atomic Coordinates and Displacement Parameters of Mg_3Pt_2

atom	site	x/a	y/b	c/z	U_{eq}[a] (Å^2)
Pt	8f	0.3750(1)	0.27358(9)	0.36175(9)	0.0099(2)
Mg1	4e	0	0.154(2)	0.25	0.014(2)
Mg2	8f	0.306(1)	0.0552(9)	0.023(1)	0.012(2)

[a] $U_{eq} = 4/3[U_{11}(a^*)^2a^2 + \ldots 2U_{23}(b^*)(c^*)bc\cos(\alpha)]$.

4.3. Structural Relationships. Mg_3Pt_2 is isotypic to Eu_3Ga_2.[74] The relevant interatomic distances in Mg_3Pt_2 are listed in Table 3. The striking feature of the crystal structure (Figure 2) is chains of Pt atoms, with alternating Pt−Pt distances. The shorter distance d_1(Pt−Pt) = 2.68 Å is smaller than the Pt−Pt contact of 2.77 Å in face-centered-cubic (fcc)

Table 3. Interatomic Distances in the Crystal Structure of Mg_3Pt_2

atoms		distance (Å)	CN
Pt	Mg1	2.630(2)	
	Mg2	2.651(7)	
	Pt	2.677(1)	
	Mg2	2.712(7)	
	Mg2	2.715(6)	
	Mg1	2.736(3)	11
	Mg2	2.745(6)	
	Mg2	2.889(6)	
	Pt	2.984(1)	
	Mg1	3.046(9)	
	Mg2	3.244(7)	
Mg1	2 Pt	2.630(2)	
	2 Pt	2.736(3)	
	2 Mg2	2.897(9)	
	2 Pt	3.046(9)	
	2 Mg2	3.126(7)	14
	2 Mg2	3.362(9)	
	2 Mg2	3.392(11)	
Mg2	Pt	2.651(7)	
	Pt	2.712(7)	
	Pt	2.715(6)	
	Pt	2.745(6)	
	Pt	2.889(6)	
	Mg1	2.897(9)	
	Mg2	2.911(9)	
	Mg2	2.997(10)	
	Mg1	3.126(7)	15
	Pt	3.244(7)	
	Mg1	3.362(9)	
	Mg1	3.392(11)	
	2 Mg2	3.539(9)	
	Mg2	3.571(9)	

https://doi.org/10.1021/acs.inorgchem.1c01995
Inorg. Chem. 2021, 60, 13681−13690

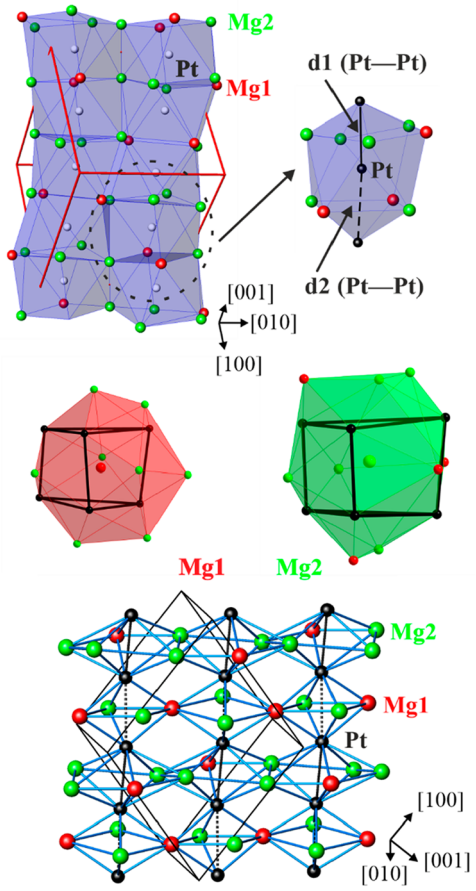

Figure 2. Crystal structures of Mg_3Pt_2. (top left) Undulating columns of distorted face-sharing [$PtMg_9$] polyhedra. For simplicity, only two metal chains are drawn; the unit cell is highlighted in red. (top right) Coordination polyhedron of Pt. (middle) Coordination polyhedra of Mg1 and Mg2. (bottom) Interconnection of adjacent Pt chains through the sharing of vertices and edges of distorted octahedra $Pt_2(Mg1)_2(Mg2)_2$ and distorted pentagonal bipyramids $Pt_2(Mg1)$-$(Mg2)_4$.

Pt,[90] and the longer distance d_2(Pt−Pt) amounts to 2.98 Å. A comparison between d_1/d_2 ratios for the Pt atoms in the Mg_3Pt_2 structure and the Ga atoms in the isotypic Eu_3Ga_2 structure[74] shows that this ratio is smaller in Eu_3Ga_2 because of the much longer d_2 Ga−Ga distances. Therefore, only Ga−Ga dumbbells are formed, while in Mg_3Pt_2, distorted Pt chains are present. Moreover, the chains in Mg_3Pt_2 are undulating with an angle slightly less than 180°. The Pt atom is located at the center of a distorted antiprism with coordination number (CN) = 11, in which nine Mg atoms form the two basal faces of the polyhedron, which is additionally capped by two Pt atoms. Such distorted [$PtMg_9$] polyhedra are condensed by sharing faces and forming infinite undulating columns (Figure 2, top left). These columns can also be understood as being built from vertex-sharing distorted [$Pt_2(Mg1)_2(Mg2)_2$] octahedra and pentagonal [$Pt_2Mg1(Mg2)_4$] bipyramids (Figure 2, bottom). The coordination polyhedra around the Mg1 and Mg2 atoms can be described as distorted trigonal prisms formed by Pt atoms capped by Mg with CNs of 14 and 15, respectively (Figure 2, middle).

From a structural chemical perspective, Mg_3Pt_2 belongs to the Eu_3Ga_2 family. The latter can be structuraly related to the orthorhombic structures of W_2CoB_2[91] and monoclinic Ca_2SiIr_2.[92] If the atomic positions in Mg_3Pt_2 are shifted (Table S2 and Figure S3), an orthorhombic cell can be constructed (Figure 3, bottom). The atomic decoration of such

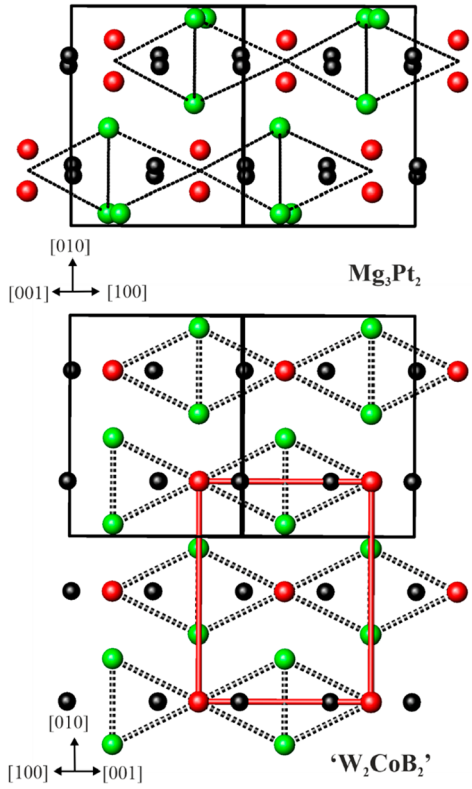

Figure 3. (top) Projection of the unit cell of Mg_3Pt_2 along the [101] direction. (bottom) Idealized atomic positions and the orthorhombic W_2CoB_2-type unit cell (red lines). Pt, Mg1, and Mg2 atoms are drawn in black, red, and green, respectively.

a cell corresponds to a binary variant of the orthorhombic W_2CoB_2 type, where Mg atoms take the place of the two transition metals and the Pt atom replaces the B atom.

Several compounds belonging to the W_2CoB_2 structural family are reported in the literature (Figure 4). They comprise different combinations of elements, bonding situations, and distance ratios d_1/d_2 in the chain. They can be described in terms of layered structures with atoms embedded between the layers. In W_2CoB_2,[91] the dumbbells of B atoms [d_1(B−B) = 1.82 Å] are aligned in the [010] direction and bridged by four Co atoms. The distance d_2(B−B) = 2.74 Å is too long to expect an interaction between B atoms. This leads to the formation of layers {CoB_2} separated by W atoms. A different situation is observed in K_2Au_3[93] and Ca_2GaCu_2.[94,95] The Au2 and Cu atoms form a continuous chain along [010] with alternating short and long distances, d_1(Au2−Au2) = 2.68 Å, and the longest distance is d_2(Au2−Au2) = 2.76 Å, respectively. In Ca_2GaCu_2, these two distances are 2.70 and 2.78 Å, respectively. In K_2Au_3, the distances d_1 and d_2 are both shorter than the shortest distances in elemental metallic Au (2.88 Å),[90] pointing out the presence of Au chains in the structure. In Ca_2GaCu_2, the distances d_1 and d_2 are both longer than the normal Cu−Cu covalent bond distance of 2.55 Å,[90] but they are still in a range in which one can expect Cu−Cu interaction. The layers of {$Au1Au2_2$}and {$GaCu_2$} are separated by the most electropositive elements K and Ca.

https://doi.org/10.1021/acs.inorgchem.1c01995
Inorg. Chem. 2021, 60, 13681−13690

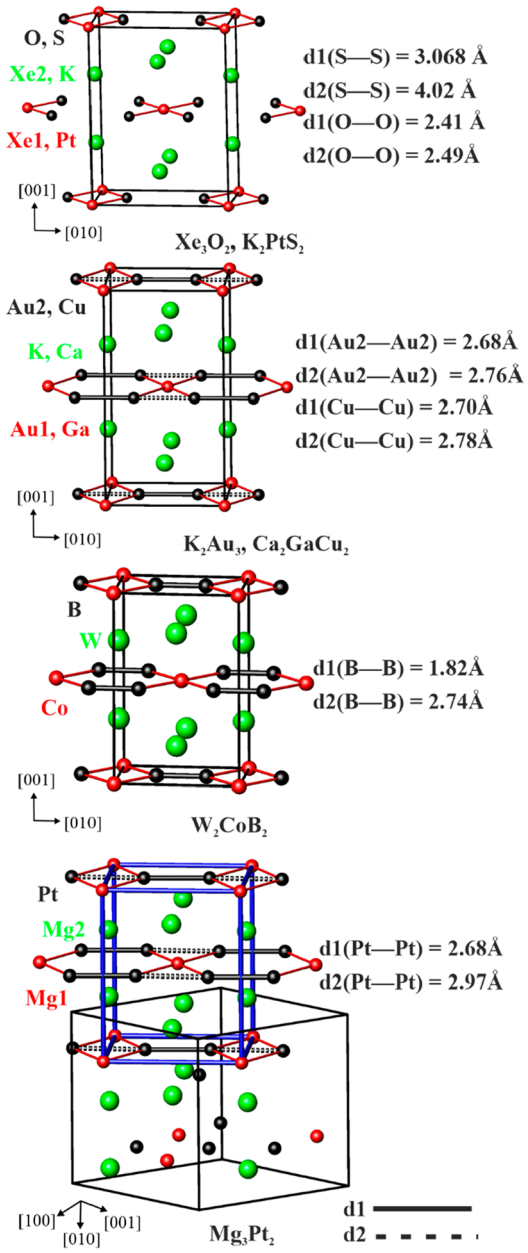

Figure 4. Comparison of orthorhombic W_2CoB_2 derivatives: d_1 (black line), shorter distances between the atoms in the chain; d_2 (dashed black line), longer distance between the atoms in the chain. The orthorhombic cell in Mg_3Pt_2 is highlighted in blue.

Finally, in Xe_3O_2[96] and K_2PtS_2,[97] no bonding between S and O atoms is observed, and the structures contain XeO_4 and PtS_4 squares parallel to [010], which share O and S corners, respectively. In XeO_4, Xe1 has an oxidation number of 4+, while the Xe2 atoms intercalated between the layer are unoxidized. In K_2PtS_2, the more electropositive K is intercalating between layers of PtS_4 squares. Finally, in the idealized orthorhombic structure of Mg_3Pt_2, Pt chains with alternating distances are observed. From a structural point of view, the situation in Mg_3Pt_2 is similar to that observed in K_2Au_3, but the composition in K_2Au_3 is "inverted" compared to that of Mg_3Pt_2. Moreover, while in K_2Au_3 the layers of Au atoms only are separated by the electropositive K, in Mg_3Pt_2 the mixed {Mg1Pt2} layers are separated by Mg2 atoms. Anionic chains of the late transition-metal atoms are observed in a structurally related family of intermetallic compounds belonging to the Ca_2SiIr_2 type:[92] Ca_2GePt_2 and Eu_2GaPt_2.[98,99] While the space group is the same for the families ($C2/c$), in the latter ternary compounds, the metal chains are stacked along [001], being almost perpendicular to each other and bridged by Ga (Si and Ge) atoms (Figure 5, right). This is

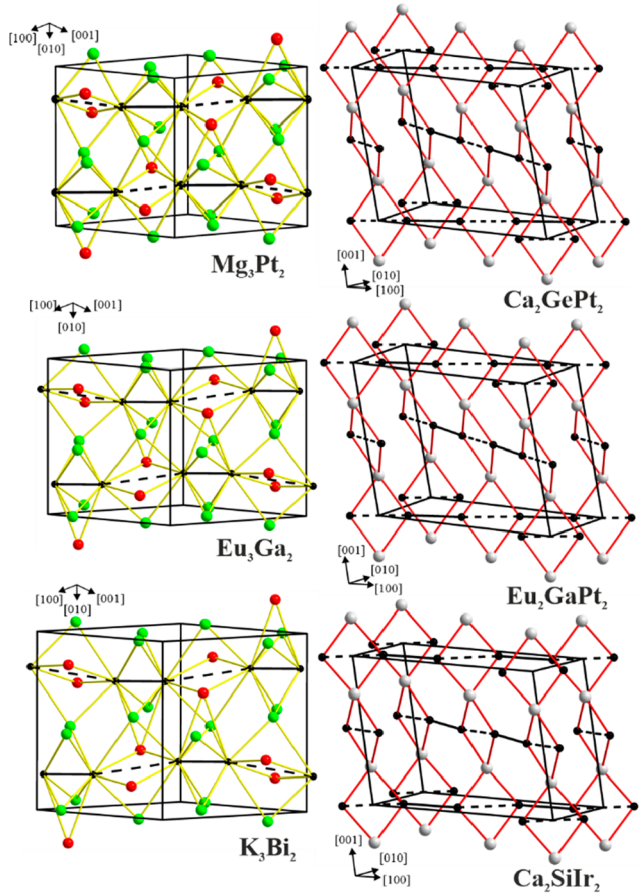

Figure 5. (left) Parallel metal chains in binary compounds of the Eu_3Ga_2 type with Mg1, Eu, and K cations acting as bridges between two parallel chains. (right) Almost perpendicular metal chains stacked along [001] in the compounds isotypic to Ca_2SiIr_2 bridged by Ga (Si and Ge) atoms.

different from the almost parallel chains observed in Mg_3Pt_2, Eu_3Ga_2,[74] and K_3Bi_2,[75] where the Mg, Eu, and K atoms act as bridges between two parallel chains (Figure 5, left).

4.4. Chemical Bonding. From the crystallographic point of view, the crystal structure of Mg_3Pt_2 can be described in different ways, depending on the structural arrangement that is used for comparison (see above). In order to gain more insight into which of this description has its roots in the atomic interactions, analysis of the chemical bonding is performed by applying the electron localizability approach, a quantum-chemical technique operating in the position space. Topological analysis of the electronic density following the QTAIM theory yields the shapes of the constituting atoms (Figure 6, top panel). Integration of the ED within these atomic basins results in the effective charges of −2.2 for Pt and +1.4 and +1.5 for the two symmetry-independent Mg species Mg1 and Mg2, respectively. The essential charge transfer is in agreement with

https://doi.org/10.1021/acs.inorgchem.1c01995
Inorg. Chem. 2021, 60, 13681−13690

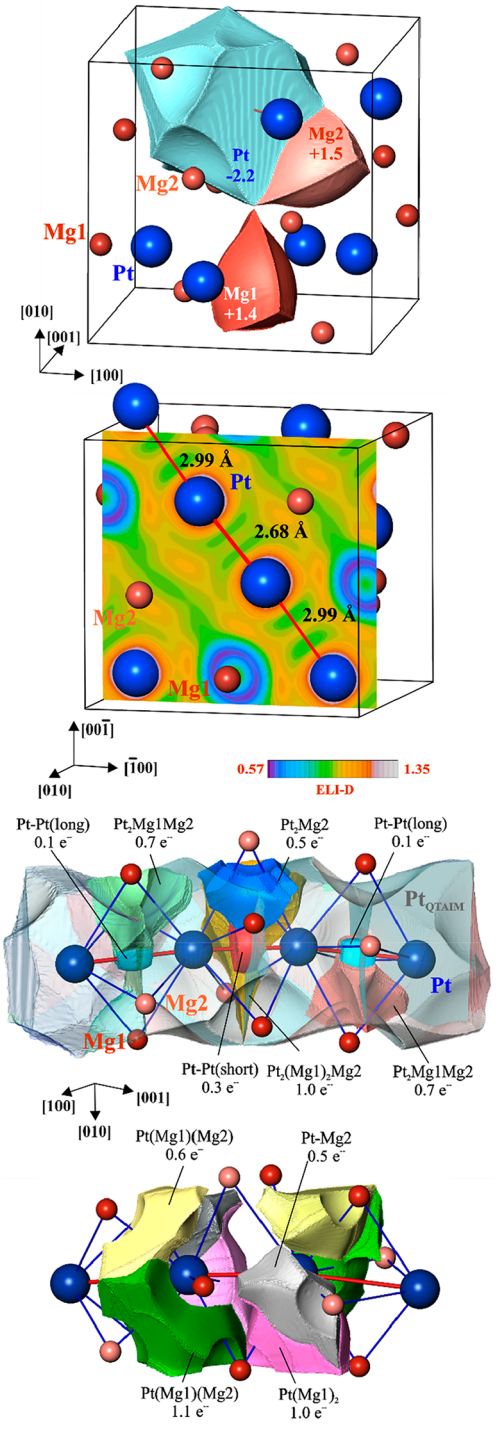

Figure 6. Chemical bonding in Mg_3Pt_2: (top) shapes of the QTAIM atoms and their charges; (upper middle panel) ELI-D distribution in the plane of the Pt chain; (lower middle panel) ELI-D basin of the bonding interactions in the Pt chain involving two Pt atoms (color code) and the QTAIM Pt atoms (transparent); (bottom) ELI-D basin of the bonding interaction in the Pt chain involving one Pt atom.

the electronegativity difference between Pt and Mg. The shapes of the Mg cations are similar to the Be species in $Be_{21}Pt_5$[100] and Be_5Pt[101] and show clear deviation from a sphere (including mainly the inner shells), characteristic for the (formally divalent) cations, e.g., in intermetallic clathrates.[102,103] The markedly larger shape of the Pt anion contains plane faces toward the Pt neighbors and concave faces toward the cations, indicating interactions of different polarities. Analysis of the literature information reveals only five binary compounds belonging to the Eu_3Ga_2 type.[74] Besides the prototype and Mg_3Pt_2, this family includes three bismuthides of alkaline metals, K_3Bi_2, Rb_3Bi_2, and Cs_3Bi_2.[75] QTAIM analysis of the ED for Eu_3Ga_2 and K_3Bi_2 confirms the important role of charge transfer for stabilization of the atomic arrangement of this type (Figure 7, top panel). Nevertheless,

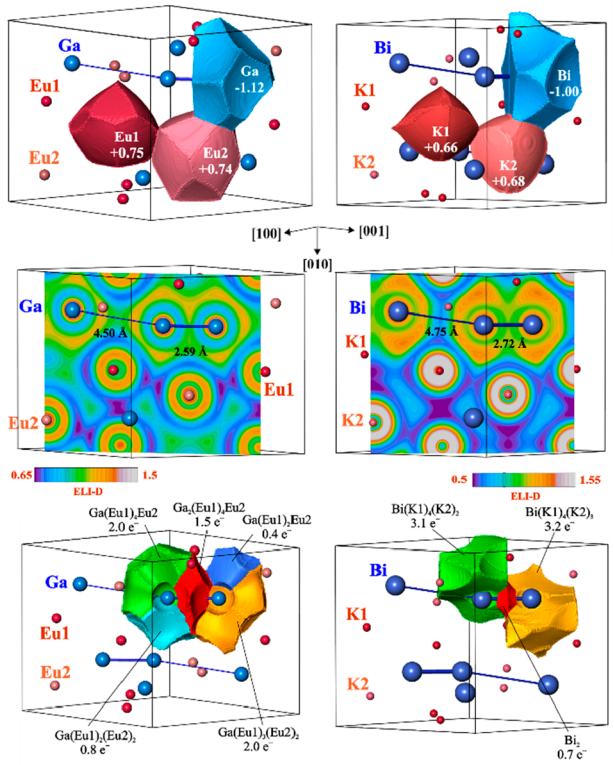

Figure 7. Chemical bonding in Eu_3Ga_2 (left) and K_3Bi_2 (right): (top) QTAIM atoms and their effective charges; (middle) ELI-D distribution in the plane of the Ga or Bi chains; (bottom) ELI-D basins of bonding interactions involving Ga or Bi atoms.

the absolute charge values are noticeably smaller in comparison with Mg_3Pt_2 (cf. −1.12 for Ga and −1.0 for Bi with the approximately double negative charge of Pt).

Distribution of the ELI in Mg_3Pt_2 reveals maxima in the vicinity of the Pt chains with alternating Pt−Pt distances (Figure 6, upper middle panel). They can be classified in three groups. The one group visualizes the Pt−Pt interactions (red and light blue in the lower middle panel in Figure 6), confirming the formation of a Pt chain. These basins remain also after optimization of the structure (cf. Calculation Procedures). The populations of these basins are rather low (0.1−0.3 e^-), indicating that they do not seem to play a key role. This function carries multiatomic interactions of the second and third kinds. The basins of the second kind of attractors have contact with the core basins of two neighboring Pt atoms and other Mg species. They visualize the multiatomic interactions "bridging" the Pt−Pt bonds (Figure 6, lower middle panel). The attractors of the third group reveal the three- and two-atomic interactions with Mg involving one Pt atom only (Figure 6, bottom panel). The basin populations of the second and third groups of attractors (0.5−1.1 e^-) are essentially larger than that of the Pt−Pt bonds. Thus, the Pt

https://doi.org/10.1021/acs.inorgchem.1c01995
Inorg. Chem. 2021, 60, 13681−13690

chain in Mg_3Pt_2 is stabilized by a complex system of two-, three-, and four-atomic bonds involving Pt species from the chains. The intersection of these bond basins with the QTAIM atomic basins of Pt clearly shows that the latter contribute the majority of the populations; i.e., all interactions involving Pt and Mg are strongly polar. The presence of numerous multiatomic interactions in the structure correlate with the calculated electronic density of states (DOS; Figure S2), which is mainly formed by the Pt *d* states with small contributions of the Mg *s* states and has a low but nonnegligible DOS at the Fermi level. The experimentally found metallic behavior of Mg_3Pt_2 is also in line with the DOS (Figure S4).

Topological analysis of ELI-D for Eu_3Ga_2 yields, despite the same structure type, an essentially different bonding picture (Figure 7, left middle and bottom panels). A two-atomic Ga−Ga interaction is observed only for the shorter Ga−Ga contact. Its basin has a population of 1.5 e^-, being much larger in comparison to the Pt−Pt bonds in Mg_3Pt_2. Besides the major contributions of two Ga atoms to the basin, also a small portion comes from the five bridging Eu species. The remaining basins (four for each Ga) involve each contribution from one Eu and several Ga atoms and visualize lone-pair-like multiatomic bonding. In total, chemical bonding in Eu_3Ga_2 reveals, within the "chain", the formation of separated Ga_2 dumbbells with bridged Ga−Ga bonds. The dumbbells are separated by multicenter lone-pair-like interactions. The next representative of the Eu_3Ga_2 type, K_3Bi_2, is also characterized by the formation of Bi2 dumbbells (Figure 7, right middle panel). In this case, the Bi−Bi interaction is clearly a two-atomic one: only two-atomic basins of Bi contribute to the bonding basin (population of 0.7 e^-; Figure 7, right bottom panel).

Each Bi species has on the bond-opposite side two lone-pair-like basins visualizing the polar seven- and eight-atomic interactions of Bi with its K ligands. The populations of these basins (3.1 and 3.2 e^-) are the largest in the series of the three Eu_3Ga_2-type representatives studied. In summary, the common bonding feature of the Eu_3Ga_2-type representatives is the polar interaction between different components. The polarity increases with increasing electronegativity difference between the constituents. The main structural feature, the formation of a homoatomic anionic chainlike arrangement, depends on the number of available electrons per formula unit (VE). For the larger numbers (VE of 13 for K_3Bi_2 [VEC(Bi) = 6.5] and VE of 12 for Eu_3Ga_2 [VEC(Ga) = 6]), the formal chain splits into separate dumbbells. The total number of electrons in the bonding basins around the dumbbells are 13.3 and 11.9, respectively, being close to the VE values. For lower numbers of electrons available (VE = 8 in Mg_3Pt_2 [VEC(Pt) = 4]), the chain arrangement with alternating distances is stabilized. The total number of electrons in the bonding basins (per two Pt atoms) is 10.7, revealing participation of the penultimate-shell electrons of Pt in the bonding.

5. CONCLUSIONS

The binary compound Mg_3Pt_2 was obtained either by direct reaction of elemental metals or by spark-plasma treatment of mixtures of $PtCl_2$ and MgH_2. Mg_3Pt_2 is isotypic with Eu_3Ga_2 (and A_3Bi_2, where A = K, Rb, and Cs) but differs clearly from the latter compounds from the chemical bonding point of view. While, because of the sufficient number of valence electrons available, the minority atoms in Eu_3Ga_2 and A_3Bi_2 form isolated dumbbells arranged along a line with a huge difference between the short and long distances within such a "chain", the Pt atoms in Mg_3Pt_2 form almost linear chains with only moderate alternating Pt−Pt distances in the chain. Analysis of the chemical bonding reveals multiatomic interactions stabilizing the Pt−Pt chain, while the dumbbells in Eu_3Ga_2 and A_3Bi_2 are separated within the line by "lone pairs" (strongly polar multiatomic interactions). The metallic and diamagnetic character of Mg_3Pt_2 is confirmed by physical property measurements.

■ ASSOCIATED CONTENT

Supporting Information

The Supporting Information is available free of charge at https://pubs.acs.org/doi/10.1021/acs.inorgchem.1c01995.

Anisotropic displacement parameters, thermal analysis, calculated DOS, idealized coordinates for Mg_3Pt_2, and physical properties (PDF)

Accession Codes

CCDC 2089451 contains the supplementary crystallographic data for this paper. These data can be obtained free of charge via www.ccdc.cam.ac.uk/data_request/cif, or by emailing data_request@ccdc.cam.ac.uk, or by contacting The Cambridge Crystallographic Data Centre, 12 Union Road, Cambridge CB2 1EZ, UK; fax: +44 1223 336033.

■ AUTHOR INFORMATION

Corresponding Author

Andreas Leithe-Jasper − *Max-Planck-Institut für Chemische Physik fester Stoffe, Dresden 01187, Germany;* orcid.org/0000-0001-7688-4365; Email: Andreas.Leithe-Jasper@cpfs.mpg.de

Authors

Laura Agnarelli − *Max-Planck-Institut für Chemische Physik fester Stoffe, Dresden 01187, Germany*

Yurii Prots − *Max-Planck-Institut für Chemische Physik fester Stoffe, Dresden 01187, Germany;* orcid.org/0000-0002-7418-9892

Ulrich Burkhardt − *Max-Planck-Institut für Chemische Physik fester Stoffe, Dresden 01187, Germany*

Marcus Schmidt − *Max-Planck-Institut für Chemische Physik fester Stoffe, Dresden 01187, Germany*

Primož Koželj − *Max-Planck-Institut für Chemische Physik fester Stoffe, Dresden 01187, Germany*

Yuri Grin − *Max-Planck-Institut für Chemische Physik fester Stoffe, Dresden 01187, Germany;* orcid.org/0000-0003-3891-9584

Complete contact information is available at: https://pubs.acs.org/10.1021/acs.inorgchem.1c01995

Author Contributions

The manuscript was written through contributions of all authors. All authors have given approval to the final version of the manuscript.

Funding

Open access funded by Max Planck Society.

Notes

The authors declare no competing financial interest.

■ ACKNOWLEDGMENTS

The authors are grateful to Dr. F. R. Wagner and Dr. A. Ormeci for helpful discussions. We thank Dr. H. Borrmann and S. Hückmann for PXRD measurements, S. Kostmann, P. Scheppan, and M. Eckert for metallographic characterization of the samples, and S. Scharsach for DSC measurements. We are also thankful to K. Vanatko for help in the sample preparation and Dr. Igor Veremchuk and F. Kaiser for their suggestions concerning the SPS technique. We thank I. Werner for help with information searches.

■ REFERENCES

(1) Mordike, B. L.; Ebert, T. Magnesium - Properties - applications - potential. *Mater. Sci. Eng., A* **2001**, *302* (1), 37−45.
(2) Kaiser, F.; Kainer, K. U. The Current State of Technology and Potential for further Development of Magnesium Applications. *Magnesium Alloys and Technology*; John Wiley & Sons, 2003; p 285.
(3) Abbott, T. B. Magnesium: Industrial and Research Developments Over the Last 15 Years. *Corrosion* **2015**, *71* (2), 120−127.
(4) Kulekci, M. K. Magnesium and its alloys applications in automotive industry. *Int. J. Adv. Manuf. Technol.* **2008**, *39* (9), 851−865.
(5) Bamberger, M.; Dehm, G. Trends in the development of new Mg alloys. *Annu. Rev. Mater. Res.* **2008**, *38*, 505−533.
(6) Polmear, I.; St. John, D.; Nie, J.-F.; Qian, M. *Light Alloys: Metallurgy of the Light Metals*; Butterworth-Heinemann, Elsevier: Oxford, U.K., 2017; p 525.
(7) You, S. H.; Huang, Y. D.; Kainer, K. U.; Hort, N. Recent research and developments on wrought magnesium alloys. *J. Magnesium Alloys* **2017**, *5* (3), 239−253.
(8) Mo, N.; Tan, Q. Y.; Bermingham, M.; Huang, Y. D.; Dieringa, H.; Hort, N.; Zhang, M. X. Current development of creep-resistant magnesium cast alloys: A review. *Mater. Des.* **2018**, *155*, 422−442.
(9) Ramalingam, V. V.; Ramasamy, P.; Kovukkal, M. D.; Myilsamy, G. Research and Development in Magnesium Alloys for Industrial and Biomedical Applications: A Review. *Met. Mater. Int.* **2020**, *26* (4), 409−430.
(10) Pekgüleryüz, M. O.; Kainer, K.; Kaya, A. A. *Fundamentals of Magnesium Alloy Metallurgy*; Elsevier, 2013; p 368.
(11) Priya, P.; Yan, X. L.; Chaudhuri, S. Study of intermetallics for corrosion and creep resistant microstructure in Mg-RE and Mg-Al-RE alloys through a data-centric high-throughput DFT framework. *Comput. Mater. Sci.* **2020**, *175*, 109541.
(12) Schwarz, R. B. Hydrogen Storage in Magnesium-Based Alloys. *MRS Bull.* **1999**, *24* (11), 40−44.
(13) Crivello, J. C.; Dam, B.; Denys, R. V.; Dornheim, M.; Grant, D. M.; Huot, J.; Jensen, T. R.; de Jongh, P.; Latroche, M.; Milanese, C.; Milčius, D.; Walker, G. S.; Webb, C. J.; Zlotea, C.; Yartys, V. A. Review of magnesium hydride-based materials: development and optimization. *Appl. Phys. A: Mater. Sci. Process.* **2016**, *122* (2), 97.
(14) Pasquini, L. The Effects of Nanostructure on the Hydrogen Sorption Properties of Magnesium-Based Metallic Compounds: A Review. *Crystals* **2018**, *8* (2), 106.
(15) Staiger, M. P.; Pietak, A. M.; Huadmai, J.; Dias, G. Magnesium and its alloys as orthopedic biomaterials: A review. *Biomaterials* **2006**, *27* (9), 1728−1734.
(16) Riaz, U.; Shabib, I.; Haider, W. The current trends of Mg alloys in biomedical applications-A review. *J. Biomed. Mater. Res., Part B* **2019**, *107* (6), 1970−1996.
(17) Vej-Hansen, U. G.; Escudero-Escribano, M.; Velázquez-Palenzuela, A.; Malacrida, P.; Rossmeisl, J. L.; Stephens, I. E. L.; Chorkendorff, I.; Schiøtz, J. New Platinum Alloy Catalysts for Oxygen Electroreduction Based on Alkaline Earth Metals. *Electrocatalysis* **2017**, *8* (6), 594−604.
(18) Tetteh, E. B.; Lee, H.-Y.; Shin, C.-H.; Kim, S.-h.; Ham, H. C.; Tran, T.-N.; Jang, J.-H.; Yoo, S. J.; Yu, J.-S. New PtMg Alloy with Durable Electrocatalytic Performance for Oxygen Reduction Reaction in Proton Exchange Membrane Fuel Cell. *ACS Energy Lett.* **2020**, *5* (5), 1601−1609.
(19) Okabe, T. H.; Yamamoto, S.; Kayanuma, Y.; Maedaaff, M. Recovery of platinum using magnesium vapor. *J. Mater. Res.* **2003**, *18* (8), 1960−1967.
(20) Emley, E. *Principles of Magnesium Technology*; Pergamon Press: New York or London, 1966.
(21) Pöttgen, R.; Hoffmann, R. D. The role of magnesium in intermetallics and related compounds. *Metall.* **2004**, *58* (9), 557−561.
(22) Hort, N.; Huang, Y. D.; Kainer, K. U. Intermetallics in magnesium alloys. *Adv. Eng. Mater.* **2006**, *8* (4), 235−240.
(23) Boom, R.; de Boer, F. Enthalpy of formation of binary solid and liquid Mg alloys−Comparison of Miedema-model calculations with data reported in literature. *CALPHAD: Comput. Coupling Phase Diagrams Thermochem.* **2020**, *68*, 101647.
(24) De Negri, S.; Giovannini, M.; Saccone, A. Phase relationships of the La−Ni−Mg system at 500°C from 0 to 66.7 atom % Ni. *J. Alloys Compd.* **2005**, *397* (1), 126−134.
(25) Heying, B.; Hoffmann, R. D.; Pottgen, R. Structure refinement of the S-phase precipitate $MgCuA_{l2}$. *Z. Naturforsch., B: J. Chem. Sci.* **2005**, *60* (5), 491−494.
(26) De Negri, S.; Giovannini, M.; Saccone, A. Constitutional properties of the La−Cu−Mg system at 400°C. *J. Alloys Compd.* **2007**, *427* (1), 134−141.
(27) Rodewald, U. C.; Chevalier, B.; Pottgen, R. Rare earth-transition metal-magnesium compounds - An overview. *J. Solid State Chem.* **2007**, *180* (5), 1720−1736.
(28) De Negri, S.; Solokha, P.; Saccone, A.; Pavlyuk, V. The Y−Cu−Mg system in the 0−66.7 atom % Cu concentration range: The isothermal section at 400°C. *Intermetallics* **2009**, *17* (8), 614−621.
(29) Solokha, P.; De Negri, S.; Pavlyuk, V.; Saccone, A. Anti-Mackay Polyicosahedral Clusters in La-Ni-Mg Ternary Compounds: Synthesis and Crystal Structure of the $La_{43}Ni_{17}Mg_5$ New Intermetallic Phase. *Inorg. Chem.* **2009**, *48* (24), 11586−11593.
(30) Solokha, P.; De Negri, S.; Pavlyuk, V.; Saccone, A. Crystal chemical peculiarities of rare earth (R) rich magnesium intermetallic compounds in R−T−Mg (T= transition element) systems. *Chem. Met. Alloys* **2009**, *2* (1/2), 39−48.
(31) Ourane, B.; Gaudin, E.; Zouari, R.; Couillaud, S.; Bobet, J.-L. $NdNiMg_5$, a new magnesium-rich phase with an unusual structural type. *Inorg. Chem.* **2013**, *52* (23), 13289−13291.
(32) Jin, Q.-Q.; Mi, S.-B. Intermetallic phases in Mg−Co−Y alloys. *J. Alloys Compd.* **2014**, *582*, 130−134.
(33) Villars, P.; Cenzual, K.; Pearson, W. B. *Pearson's Crystal Data: Crystal Structure Database for Inorganic Compounds*; ASM International: Novelty, OH, 2016.
(34) Stein, S.; Heletta, L.; Pöttgen, R. Equiatomic compounds REIrMg (RE = Y, La-Nd, Sm, Gd-Tm) and RERhMg (RE = Y, Sm, Gd-Tm). *J. Solid State Chem.* **2017**, *253*, 184−191.
(35) Stein, S.; Heletta, L.; Block, T.; Pöttgen, R. Rare earth-copper-magnesium intermetallics: crystal structure of CeCuMg, magnetocaloric effect of GdCuMg and physical properties of the Laves phases $RECu_4Mg$ (RE = Sm, Gd, Tb, Tm). *Z. Naturforsch., B: J. Chem. Sci.* **2018**, *73* (12), 987−997.
(36) Zhang, Z.; Stein, S.; Li, L.; Pöttgen, R. Magnetocaloric effect and critical behavior in ternary equiatomic magnesium compounds *RE*PtMg (*RE* = Tb, Dy and Ho). *Intermetallics* **2019**, *109*, 24−29.
(37) Freccero, R.; De Negri, S.; Saccone, A.; Solokha, P. Solid state interactions in the La−Au−Mg system: phase equilibria, novel compounds and chemical bonding. *Dalton Trans.* **2020**, *49* (34), 12056−12067.
(38) De Boer, F. R.; Mattens, W.; Boom, R.; Miedema, A.; Niessen, A. Cohesion in metals. *Transition Metal Alloys*; Elsevier Scientific Pub. Co.: Amsterdam, NY, 1988; Vol. *1*.
(39) Nayeb-Hashemi, A. A.; Clark, J. B. *Phase Diagrams of Binary Magnesium Alloys*; American Society for Metals: Metals Park, OH, 1988.
(40) Massalski, T. B.; Murray, J. L.; Bennett, L. H.; Baker, H. *Binary Alloy Phase Diagrams*; ASM International: Novelty, OH, 1986; Vol. *2*.

https://doi.org/10.1021/acs.inorgchem.1c01995
Inorg. Chem. 2021, 60, 13681−13690

(41) Ferro, R.; Rolla, S. L. *Atti Accad. Naz. Lincei, Cl. Sci. Fis., Mat. Nat., Rend.***1960**, *29*, 70−73.
(42) Westin, L. Crystal structure of Rh_7Mg_{44}. *Chem. Scr.* **1971**, *1* (3), 127.
(43) Westin, L.; Edshammar, L. E.; Leijonmarck, M.; Mikhaiel, S. A.; Engebretsen, J. E.; Ehrenberg, L. On the Crystal Structure of $RhMg_6$. *Acta Chem. Scand.* **1971**, *25* (4), 1480.
(44) Andersson, S. An alternative description of the structures of Rh_7Mg_{44} and Mg_6Pd. *Acta Crystallogr., Sect. A: Cryst. Phys., Diffr., Theor. Gen. Crystallogr.* **1978**, *34* (6), 833−835.
(45) Bonhomme, F.; Selvam, P.; Yoshida, M.; Yvon, K.; Fischer, P. Hydrogen-stabilized $Mg_2RhH_{1.1}$ with filled Ti_2Ni-type structure. *J. Alloys Compd.* **1992**, *178* (1), 167−172.
(46) Hlukhyy, V.; Rodewald, U. C.; Hoffmann, R.-D.; Pöttgen, R. Synthesis and Structure of $RhMg_3$ and Ir_3Mg_{13}. *Z. Naturforsch., B: J. Chem. Sci.* **2004**, *59* (3), 251−255.
(47) Ferro, R.; Rambaldi, G.; Capelli, R. Research on the alloys of noble metals with the more electropositive elements V. Micrographic and X-ray examination of some magnesium-iridium alloys. *J. Less-Common Met.* **1962**, *4* (1), 16−23.
(48) Westin, L.; Edshammar, L. E.; Krogh-Moe, J.; Songstad, J.; Pilotti, Å The Crystal structure of Ir_7Mg_{44}. *Acta Chem. Scand.* **1972**, *26* (9), 3619−3626.
(49) Range, K.-J.; Hafner, P. Structure Refinement of $AuMg_3$, $IrMg_3$ and $IrMg_{2.8}$. *J. Alloys Compd.* **1993**, *191*, L5−L7.
(50) Kreiner, G.; Franzen, H. F. A new cluster concept and its application to quasi-crystals of the i-AlMnSi family and closely related crystalline structures. *J. Alloys Compd.* **1995**, *221* (1), 15−36.
(51) Cerny, R.; Renaudin, G.; Favre-Nicolin, V.; Hlukhyy, V.; Pottgen, R. $Mg_{1+x}Ir_{1-x}$ (x = 0, 0.037 and 0.054), a binary intermetallic compound with a new orthorhombic structure type determined from powder and single-crystal X-ray diffraction. *Acta Crystallogr., Sect. B: Struct. Sci.* **2004**, *60* (3), 272−281.
(52) Hlukhyy, V.; Pöttgen, R. The Hexagonal Laves Phase $MgIr_2$. *Z. Naturforsch., B: J. Chem. Sci.* **2004**, *59* (8), 943−946.
(53) Hlukhyy, V.; Pöttgen, R. $Mg_{2+x}Ir_{3-x}$ (x = 0.30)—a binary variant of the monoclinic $V2(Co_{0.57}Si_{0.43})_3$ type. *Solid State Sci.* **2004**, *6* (10), 1175−1180.
(54) Ferro, R. Research on the alloys of noble metals with the more electropositive elements: II. Micrographic and roentgenographic examination of the magnesium-palladium alloys. *J. Less-Common Met.* **1959**, *1* (6), 424−438.
(55) Kripyakevich, P.; Gladyshevskii, E. Crystal Structures of some compounds of Palladium with Magnesium. *Sov. Phys. Crystallogr.* **1960**, *5*, 552−554.
(56) Stadelmaier, H. H.; Hardy, W. K. Ternare Kohlenstofflegierungen von Palladium und Platin mit Magnesium, Aluminium, Zink, Gallium, Germanium, Kadmium, Indium, Zinn, Quecksilber, Thallium und Blei. *Int. J. Mater. Res.* **1961**, *52* (6), 391−396.
(57) Westin, L.; Folkmarson, L.; Olofsson, B.; Nielsen, P. H. A Palladium-Magnesium alloy phase f Co_2Al_5 type. *Acta Chem. Scand.* **1968**, *22* (8), 2574.
(58) Sampson, S. Complex cubic A_6B compounds. II. The crystal structure of Mg_6Pd. *Acta Crystallogr., Sect. B: Struct. Crystallogr. Cryst. Chem.* **1972**, *28* (3), 936−945.
(59) Wannek, C.; Harbrecht, B. Structure and Thermal Stability of the New Intermetallics $MgPd_2$, $MgPd_3$, and Mg_3Pd_5 and the Kinetics of the Iodine-Catalyzed Formation of $MgPd_2$. *J. Solid State Chem.* **2001**, *159* (1), 113−120.
(60) Makongo, J. P. A.; Kudla, C.; Prots, Y.; Niewa, R.; Burkhardt, U.; Kreiner, G. Crystal structure of trimagnesium monopalladium, Mg_3Pd. *Z. Kristallogr. - New Cryst. Struct.* **2005**, *220* (1−4), 309−310.
(61) Makongo, J. P. A.; Prots, Y.; Burkhardt, U.; Niewa, R.; Kudla, C.; Kreiner, G. A case study of complex metallic alloy phases: structure and disorder phenomena of Mg−Pd compounds. *Philos. Mag.* **2006**, *86* (3−5), 427−433.
(62) Delsante, S.; Novakovic, R.; Gagliolo, A.; Borzone, G. Thermodynamic investigation on the Mg−Pd intermetallic phases. *J. Chem. Thermodyn.* **2019**, *139*, 105890.
(63) Gierlotka, W.; Dębski, A.; Terlicka, S.; Gąsior, W.; Pęska, M.; Polański, M. Insight into Phase Stability in the Mg-Pd System: The Ab Initio Calculations. *J. Phase Equilib. Diffus.* **2020**, *41* (5), 681−686.
(64) Salvador, J. R.; Herbst, J. F.; Meyer, M. S. Synthesis and hydriding behavior of Li_2MgPt. *J. Alloys Compd.* **2011**, *509* (6), 2650−2653.
(65) Ferro, R.; Rambaldi, G. Research on the alloys of noble metals with the more electropositive elements: III. Micrographic and X-ray examination of some magnesium-platinum alloys. *J. Less-Common Met.* **1960**, *2* (5), 383−391.
(66) Range, K.-J.; Hafner, P. A redetermination of the crystal structure of trimagnesium platinum, Mg_3Pt. *J. Alloys Compd.* **1992**, *183*, 430−437.
(67) Schmitt, R.; Glaser, J.; Meyer, H.-J. The New Ternary Boride Mg_8Pt_4B and the New Intermetallic Compound $PtMg_2$. *Z. Anorg. Allg. Chem.* **2006**, *632*, 2198−2200.
(68) Bronger, W.; Klemm, W. Darstellung von Legierungen des Platins mit unedlen Metallen. *Z. Anorg. Allg. Chem.* **1962**, *319* (1−2), 58−81.
(69) Aleandri, L.; Bogdanović, B.; Wilczok, U.; Noréus, D.; Block, G. Low Temperature Synthesis and Structural Characterization of three Novel Magnesium Platinum Intermetallics, t-$MgPtC_xH_y$, t-$Mg_2PtC_xH_y$, m-$Mg_2PtC_xH_y$*. *Z. Phys. Chem.* **1994**, *185* (1), 131−144.
(70) Hyde, B. G.; Andersson, S. *Inorganic Crystal Structures*; Wiley, 1989.
(71) Eisheh, J.-T. Untersuchungen zur Thermodynamik, Konstitution und Diffusion an den Systemen Magnesium-Platin und Magnesium-Palladium. Dissertation, ChristianAlbrechtsUniversität zu Kiel, Kiel, Germany, 2006.
(72) Schmidt, J. Anwendung des Spark Plasma Sinterverfahrens für Präparationszwecke in der Festkörperchemie. Ph.D. Thesis, Technische Universität Dresden, Dresden, Germany, 2003.
(73) Akselrud, L.; Grin, Y. WinCSD: software package for crystallographic calculations (Version 4). *J. Appl. Crystallogr.* **2014**, *47* (2), 803−805.
(74) Fornasini, M. L.; Cirafici, S. Crystal-structures of Eu_3Ga_2, EuGa, Eu_2In, EuIn and $EuIn_4$. *Z. Kristallogr. - Cryst. Mater.* **1990**, *190* (3−4), 295−304.
(75) Gascoin, F.; Sevov, S. C. Synthesis and Characterization of A_3Bi_2 (A = K, Rb, Cs) with Isolated Diatomic Dianion of Bismuth, $[Bi_2]^{2-}$, and an Extra Delocalized Electron. *J. Am. Chem. Soc.* **2000**, *122* (41), 10251−10252.
(76) Koepernik, K.; Eschrig, H. Full-potential nonorthogonal local-orbital minimum-basis band-structure scheme. *Phys. Rev. B: Condens. Matter Mater. Phys.* **1999**, *59* (3), 1743−1757.
(77) Perdew, J. P.; Wang, Y. Accurate and simple analytic representation of the electron-gas correlation energy. *Phys. Rev. B: Condens. Matter Mater. Phys.* **1992**, *45* (23), 13244−13249.
(78) Kohout, M. A measure of electron localizability. *Int. J. Quantum Chem.* **2004**, *97* (1), 651−658.
(79) Wagner, F. R.; Bezugly, V.; Kohout, M.; Grin, Y. Charge decomposition analysis of the electron localizability indicator: a bridge between the orbital and direct space representation of the chemical bond. *Chem. - Eur. J.* **2007**, *13* (20), 5724−5741.
(80) Kohout, M.; Wagner, F. R.; Grin, Y. Atomic shells from the electron localizability in momentum space. *Int. J. Quantum Chem.* **2006**, *106* (7), 1499−1507.
(81) Kohout, M. Bonding indicators from electron pair density functionals. *Faraday Discuss.* **2007**, *135* (0), 43−54.
(82) Ormeci, A.; Rosner, H.; Wagner, F. R.; Kohout, M.; Grin, Y. Electron Localization Function in Full-Potential Representation for Crystalline Materials. *J. Phys. Chem. A* **2006**, *110* (3), 1100−1105.
(83) Kohout, M. *DGrid*, versions 4.6−5.0; Springer: Radebeul, Germany, 2018.
(84) Bader, R. F. W. *Atoms in molecules: A quantum theory*; Oxford University Press: Oxford, U.K., 1999.
(85) Grin, Y. *Comprehensive Inorganic Chemistry II*; Elsevier: Oxford, U.K., 2013; Vol. 2, pp 359−373.

https://doi.org/10.1021/acs.inorgchem.1c01995
Inorg. Chem. 2021, 60, 13681−13690

(86) Grin, Y.; Savin, A.; Silvi, B. *The Chemical Bond: Chemical Bonding across the Periodic Table*; Wiley-VCH, 2014; pp 345−382.
(87) Bende, D.; Wagner, F. R.; Grin, Y. 8 − N Rule and Chemical Bonding in Main-Group MgAgAs-Type Compounds. *Inorg. Chem.* **2015**, *54* (8), 3970−3978.
(88) Wagner, F. R.; Cardoso-Gil, R.; Boucher, B.; Wagner-Reetz, M.; Sichelschmidt, J.; Gille, P.; Baenitz, M.; Grin, Y. On Fe−Fe Dumbbells in the Ideal and Real Structures of $FeGa_3$. *Inorg. Chem.* **2018**, *57* (20), 12908−12919.
(89) Freccero, R.; Solokha, P.; De Negri, S.; Saccone, A.; Grin, Y.; Wagner, F. R. Polar-Covalent Bonding Beyond the Zintl Picture in Intermetallic Rare-Earth Germanides. *Chem. - Eur. J.* **2019**, *25* (26), 6600−6612.
(90) Donohue, J. *Structures of the Elements*; John Wiley and Sons: New York, 1974.
(91) Rieger, W.; Nowotny, H.; Benesovsky, F. Die kristallstruktur von W_2CoB_2 und isotypen phasen. *Monatsh. Chem.* **1966**, *97* (2), 378−382.
(92) Schoolaert, S.; Jung, W. Synthese und Kristallstrukturen der Calcium-Iridiumsilicide $Ca_3Ir_4Si_4$ und Ca_2Ir_2Si. *Z. Anorg. Allg. Chem.* **2002**, *628* (8), 1806−1810.
(93) Krieger-Beck, P.; Brodbeck, A.; Strähle, J. Synthese und Struktur von K_2Au_3, einer neuen Phase im System Kalium—Gold/ Synthesis and Structure of K_2Au_3, a New Phase in the System Potassium—Gold. *Z. Naturforsch., B: J. Chem. Sci.* **1989**, *44* (2), 237−239.
(94) Fornasini, M.; Merlo, F. The crystal structure of Ca_2Cu_2Ga, CaCuGa, $SrCu_2Ga$ and $BaCu_2Ga$. *J. Less-Common Met.* **1988**, *142*, 289−294.
(95) Kollmar, C.; Hoffmann, R. Bonding in the two-dimensional copper-gallium layer of a calcium copper gallium, Ca_2Cu_2Ga, crystal. *Inorg. Chem.* **1990**, *29* (13), 2466−2475.
(96) Dewaele, A.; Worth, N.; Pickard, C. J.; Needs, R. J.; Pascarelli, S.; Mathon, O.; Mezouar, M.; Irifune, T. Synthesis and stability of xenon oxides Xe_2O_5 and Xe_3O_2 under pressure. *Nat. Chem.* **2016**, *8* (8), 784−790.
(97) Bronger, W.; Günther, O. Darstellung und struktur von K_2PtS_2 und Rb_2PtS_2. *J. Less-Common Met.* **1972**, *27* (1), 73−79.
(98) Doverbratt, I.; Ponou, S.; Zhang, Y.; Lidin, S.; Miller, G. J. Linear Metal Chains in Ca_2M_2X (M = Pd, Pt; X = Al, Ge): Origin of the Pairwise Distortion and Its Role in the Structure Stability. *Chem. Mater.* **2015**, *27* (1), 304−315.
(99) Pöttgen, R.; Borrmann, H.; Grin, Y. Multi-Center vs. Two-Center Bonding within the Hetero-Polyanion in Eu_2GaPt_2 and its Prototype Ca_2SiIr_2. *Z. Anorg. Allg. Chem.* **2017**, *643* (21), 1338−1343.
(100) Amon, A.; Ormeci, A.; Bobnar, M.; Akselrud, L. G.; Avdeev, M.; Gumeniuk, R.; Burkhardt, U.; Prots, Y.; Hennig, C.; Leithe-Jasper, A.; Grin, Y. Cluster Formation in the Superconducting Complex Intermetallic Compound $Be_{21}Pt_5$. *Acc. Chem. Res.* **2018**, *51* (2), 214−222.
(101) Amon, A.; Svanidze, E.; Ormeci, A.; König, M.; Kasinathan, D.; Takegami, D.; Prots, Y.; Liao, Y.-F.; Tsuei, K.-D.; Tjeng, L. H.; Leithe-Jasper, A.; Grin, Y. Interplay of Atomic Interactions in the Intermetallic Semiconductor Be_5Pt. *Angew. Chem., Int. Ed.* **2019**, *58* (44), 15928−15933.
(102) Omerci, A.; Grin, Yu. *Thermoelectricity No. 6* **2015**, 16−32.
(103) Hübner, J.-M.; Prots, Y.; Schnelle, W.; Bobnar, M.; König, M.; Baitinger, M.; Simon, P.; Carrillo-Cabrera, W.; Ormeci, A.; Svanidze, E.; Grin, Y.; Schwarz, U. In-Cage Interactions in the Clathrate Superconductor Sr_8Si_{46}. *Chem. - Eur. J.* **2020**, *26* (4), 830−838.

https://doi.org/10.1021/acs.inorgchem.1c01995
Inorg. Chem. 2021, 60, 13681−13690